

PAPER • OPEN ACCESS

## Effect of Ni addition on CPP-GMR response in electrodeposited Co-Ni/Cu multilayered nanocylinders with an ultra-large aspect ratio

To cite this article: Kenta Nagao *et al* 2022 *Mater. Res. Express* **9** 075007

View the [article online](#) for updates and enhancements.

You may also like

- [Preparation and Magnetic Properties of  \$\text{Fe}\_3\text{O}\_4\$  Nanostructures Grown by Electrodeposition](#)

D. Carlier, C. Terrier, C. Arm *et al.*

- [Effect of flexoelectricity on the electroelastic fields of a hollow piezoelectric nanocylinder](#)

Zhi Yan and Liying Jiang

- [Discrete dipole approximation simulations of absorption spectra and local electric field distributions of superparamagnetic magnetite nanoparticles](#)

Benyang Wang and Shiliang Qu



## ECS Membership = Connection

**ECS membership connects you to the electrochemical community:**

- Facilitate your research and discovery through ECS meetings which convene scientists from around the world;
- Access professional support through your lifetime career;
- Open up mentorship opportunities across the stages of your career;
- Build relationships that nurture partnership, teamwork—and success!

**Join ECS!**

**Visit [electrochem.org/join](https://electrochem.org/join)**



# Materials Research Express



## PAPER

# Effect of Ni addition on CPP-GMR response in electrodeposited Co-Ni/Cu multilayered nanocylinders with an ultra-large aspect ratio

### OPEN ACCESS

RECEIVED  
3 May 2022

REVISED  
3 July 2022

ACCEPTED FOR PUBLICATION  
12 July 2022

PUBLISHED  
22 July 2022

Original content from this work may be used under the terms of the [Creative Commons Attribution 4.0 licence](#).

Any further distribution of this work must maintain attribution to the author(s) and the title of the work, journal citation and DOI.



Kenta Nagao<sup>1,2</sup>, Masamitsu Hayashida<sup>3</sup> and Takeshi Ohgai<sup>3,\*</sup> 

<sup>1</sup> Graduate School of Engineering, Nagasaki University, Bunkyo-machi 1-14, Nagasaki 852-8521, Japan

<sup>2</sup> Oshima Shipbuilding Co., Ltd., Oshima-cho 1605-1, Saikai-shi, Nagasaki 857-2494, Japan

<sup>3</sup> Faculty of Engineering, Nagasaki University, Bunkyo-machi 1-14, Nagasaki 852-8521, Japan

\* Authors to whom any correspondence should be addressed.

E-mail: [ohgai@nagasaki-u.ac.jp](mailto:ohgai@nagasaki-u.ac.jp)

**Keywords:** nanochannel, nanocylinder, multilayer, magnetoresistance, CPP-GMR, anodization, electrodeposition

## Abstract

Effect of Co–Ni alloy composition on the current perpendicular-to-plane giant magnetoresistance (CPP-GMR) response of electrochemically synthesized Co–Ni/Cu multilayered nanocylinders was studied using anodized aluminum oxide membranes (AAOM) with nanochannel diameter  $D \sim 67$  nm and length  $L \sim 70$   $\mu\text{m}$ . Co–Ni/Cu multilayered nanocylinders, which have an aspect ratio  $L/D$  of  $\sim 1,045$ , were fabricated in the AAOM nanochannel templates by utilizing a pulse-current electrochemical growth process in an electrolytic bath with  $\text{Co}^{2+}$ ,  $\text{Ni}^{2+}$  and  $\text{Cu}^{2+}$  ions. Co–Ni/Cu alternating structure with  $\text{Co}_{84}\text{Ni}_{16}$  alloy layer-thickness of 9.6 nm and Cu layer-thickness of 3.8 nm was clearly observed in a nanocylinder with a diameter of 63 nm. The alternating structure was composed from crystalline layers with preferential orientations in hcp-CoNi (002) and fcc-Cu (111). The Co–Ni/Cu multilayered nanocylinders were easily magnetized in the long axis direction because of the extremely large aspect ratio  $L/D$ . In  $\text{Co}_{84}\text{Ni}_{16}/\text{Cu}$  multilayered nanocylinders, the coercivity and squareness were  $\sim 0.46$  kOe and  $\sim 0.5$ , respectively. The CPP-GMR value was achieved up to 22.5% (at room temperature) in  $\text{Co}_{84}\text{Ni}_{16}/\text{Cu}$  multilayered nanocylinders.

## 1. Introduction

Data storage capacity in a hard disk drive (HDD) should be improved year by year because a cloud computing system has been prevailing all over the world [1]. Therefore, a highly sensitive magnetic field sensor is required for a HDD system with an enormous data storage capacity. Spintronics devices can be used for a magnetic field sensor which is used as a magnetic read-out head in a HDD system. Fert *et al* and Grünberg *et al* independently discovered the giant magnetoresistance (GMR) phenomenon during the electric current passes through the in-plane (CIP) direction of Fe/Cr multilayered thin films [2, 3]. After the innovation of CIP-GMR, Piroux *et al* and Blondel *et al* independently discovered that Co/Cu multilayered nanocylinders with GMR response during the electric current pass through the perpendicular-to-plane (CPP) direction can be fabricated by utilizing an ion-track etched polycarbonate membrane filter [4, 5] that does not need an ultra-high vacuum circumstance [6]. The aspect ratio in the normal direction to the layer's interfaces of a multilayered nanocylinder is quite larger than that of a multilayered thin film. Therefore, the resistance of a multilayered nanocylinder is very larger than that of a multilayered thin film if the applied current direction is perpendicular to the interfaces. This resistance enhancement results in the improvement for signal-to-noise (S/N) performance during detecting the CPP-GMR effect. Following the invention concerning the electrodeposited multilayered nanocylinders, several researchers have been studying the CPP-GMR effect by synthesizing the multilayered nanocylinders (Co/Cu, FeCoNi/Cu, etc) which were electrodeposited into a nanochannel template [7–11].

Usually, when the two kinds of metals such as Co and Cu are contacted, a galvanic cell will be formed due to the gap between the standard electrode potential of Co and Cu. This galvanic cell formation will enhance the electrochemical corrosion in the less-noble Co layer. Among ferromagnetic iron-group metals such as Fe, Co

and Ni, metallic Ni exhibits the best corrosion resistance performance such as Ni-based superalloys [12]. Hence, Ni addition to the Co layer will be quite effective in the corrosion resistance. Evans *et al* discovered that CPP-GMR effect of Co–Ni/Cu multilayered nanocylinders, which were synthesized into commercially available anodized aluminum oxide membranes (AAOM), strongly depended on the Cu layer thickness [13]. They reported that the CPP-GMR was achieved up to  $\sim 55\%$  at room temperature in the multilayered nanocylinders with Co–Ni layer thickness of 5.4 nm and the Cu layer thickness of 2.1 nm. Tang *et al* also found that CPP-GMR effect of Co–Ni/Cu multilayered nanocylinders, that were electrodeposited into commercially available AAOM, was affected by each layer thickness [14]. According to their report, the CPP-GMR was achieved up to  $\sim 23\%$  in the multilayered nanocylinders with the Co–Ni layer thickness of 10.2 nm and the Cu layer thickness of 4.2 nm. Moreover, Davis *et al* also revealed that Co–Ni–Fe/Cu multilayered nanocylinders were able to be electrodeposited into commercially available AAOM. They found that CPP-GMR performance was achieved up to 20% at room temperature in the multilayered nanocylinders with the Co–Ni–Fe layer thickness of 5.6 nm and the Cu layer thickness of 4.2 nm [15].

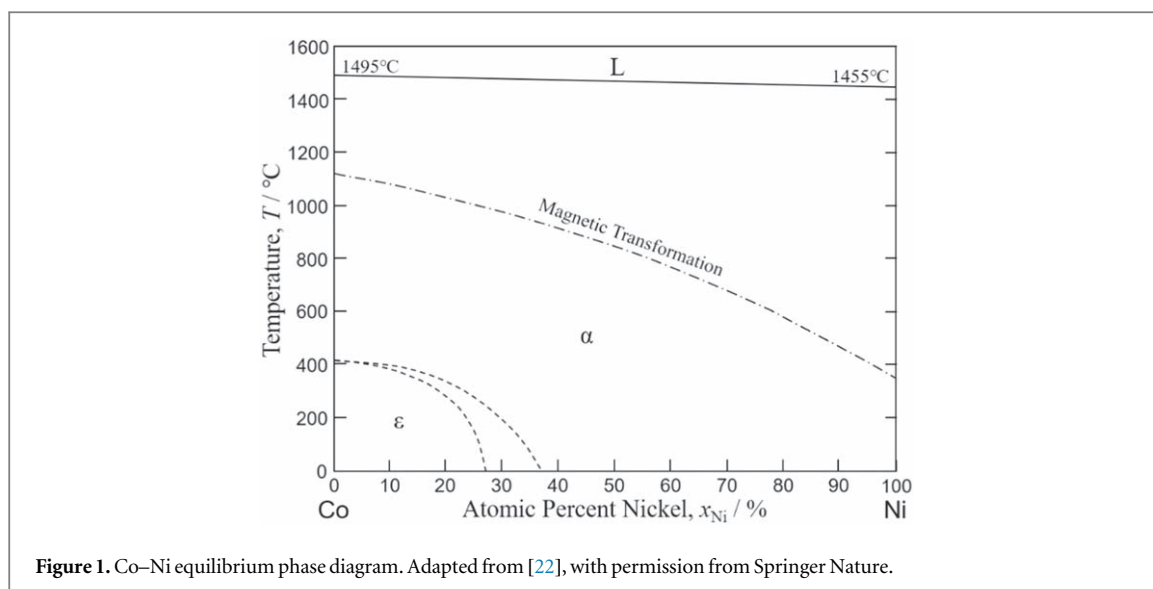
In their previous study concerning Co–Ni/Cu multilayered nanocylinders, the layer-thickness dependence on the CPP-GMR property has been investigated in detail. On the contrary, effect of Co–Ni alloy layer's composition on the CPP-GMR performance has not been revealed so far. It is predicted that the interface morphology in the multilayered structure strongly depends on the corrosion resistance performance of the electrochemically less-noble ferromagnetic layers during the pulsed current electrodeposition. Hence, it can be assumed that the Co–Ni alloy layer's composition will be affective to the quality of layers interfaces and CPP-GMR effect in the multilayered nanocylinders. Furthermore, Co–Ni/Cu multilayered nanocylinders with an ultra-large aspect ratio more than 1,000 will achieve a quite large electrical resistance more than 1 k $\Omega$  even though that is a metallic material. This resistance enhancement in a metallic material will result in the improvement for signal-to-noise (S/N) performance with a small temperature coefficient of electrical resistance in comparison with a conventional semiconductor material. On the other hand, AAOM films are quite popular as an ideal nanochannel template material for electrochemical growing nanocylinders because the nanochannel geometry, such as channel-diameter and channel-length, can be regulated by adjusting experimental conditions (e.g., anodizing voltage, current and electrolysis time) [16–19]. Therefore, in the present study, Co–Ni/Cu multilayered nanocylinders with different alloy layer's composition were synthesized in AAOM nanochannels with large aspect ratio more than 1,000. Then, the effect of Ni addition on the CPP-GMR response of electrochemically fabricated Co–Ni/Cu multilayered nanocylinders were studied.

## 2. Materials and methodology

Cross-section of a commercially available aluminum cylinder (diameter: 10 mm; length: 150 mm) was electropolished to obtain a mirror-like surface. The experimental details concerning the electropolishing condition have been described in our previous reports [20, 21]. Using an electrolytic bath (0.3 M oxalic acid containing aqueous solution), the polished cross-sectional area was anodized to make an AAOM film with numerous nanochannels. During the anodization, the cell voltage was maintained to 70 V. Following the anodization, the AAOM film was exfoliated using a specific anodic process. The experimental details concerning the exfoliation condition have been also described in our previous reports [20, 21]. To dissolve the barrier oxide layer of AAOM film, a chemical etching technique was applied to dissolve the oxide layer using an electrolytic bath (8.1 wt% phosphoric acid containing aqueous solution). The nanochannel structure of AAOM film was investigated by utilizing a scanning electron microscope (SEM). Using an argon ion (Ar<sup>+</sup>) sputter-coating system, a surface of AAOM template was sputter-deposited by a thick gold film ( $\sim 150$  nm) to cover the nanopores. Furthermore, a pure gold porous film ( $\sim 15$  nm) was also sputter-deposited on the other surface of AAOM film not to cover the nanopores. The AAOM nanochannel templates were used as a cathode electrode for electrodepositing Co–Ni/Cu multilayered nanocylinders. A pure gold wire and a silver/silver chloride (Ag/AgCl) electrode were utilized as an anode and a reference electrode, respectively. Electrolytic baths were synthesized from (0.5– $x$ ) M Co(SO<sub>3</sub>NH<sub>2</sub>)<sub>2</sub>·4H<sub>2</sub>O,  $x$  M Ni(SO<sub>3</sub>NH<sub>2</sub>)<sub>2</sub>·4H<sub>2</sub>O, 0.005 M CuSO<sub>4</sub>·5H<sub>2</sub>O, and 0.4 M H<sub>3</sub>BO<sub>3</sub>. Here,  $x$  was controlled to 0, 0.05, 0.10, 0.15, 0.20, 0.25 and 0.30 M to synthesize the electrolytic baths with 7 patterns of concentration. The solution pH and temperature were kept to pH 4 and 40 °C, respectively. Ni<sup>2+</sup> ion concentration ratio,  $R_{\text{Ni}}^{\text{bath}}$  was defined by the following equation (1).

$$R_{\text{Ni}}^{\text{bath}} = \frac{[\text{Ni}^{2+}]}{[\text{Co}^{2+}] + [\text{Ni}^{2+}]} \times 100 = \frac{x}{0.5} \times 100 \quad (1)$$

Cyclic voltammograms were investigated by utilizing an automatic polarization system to optimize the cathode potential for electrodepositing Co–Ni alloy and Cu layers. Chemical compositions of the Co–Ni alloy layers were determined by utilizing an energy-dispersive x-ray spectroscopy (EDX). Time dependence on the pulsed current



was investigated by a data logging system during growing Co–Ni/Cu multilayered nanocylinders. Following the electrochemical growth of Co–Ni/Cu nanocylinders, the AAOM templates were removed by an alkaline aqueous solution (5 M NaOH) for observing the multilayered nanocylinders using a transmission electron microscopy (TEM) to determine the thicknesses of Co–Ni alloy and Cu layers. The constituent phases of the Co–Ni/Cu multilayered nanocylinders were analyzed by utilizing an x-ray diffractometer (XRD). Magnetic hysteresis loops and magnetoresistance curves of the nanocylinders in AAOM template were investigated by utilizing a vibrating-sample magnetometer (VSM, TM-VSM1014-CRO, Tamakawa Corp., Sendai, Japan). The resistance of nanocylinders was measured by using a source meter (DC Voltage Current Source/Monitor, ADCMT6242, ADC Corp., Saitama, Japan). The magnetic field in-plane and perpendicular to the AAOM film plane was applied while increasing the field up to 10 kOe. The perpendicular magnetic field corresponds with the axial direction of nanocylinders.

### 2.1. Estimation of Ni solubility in $\epsilon$ phase (hcp-Co Alloy) using Equilibrium phase diagram

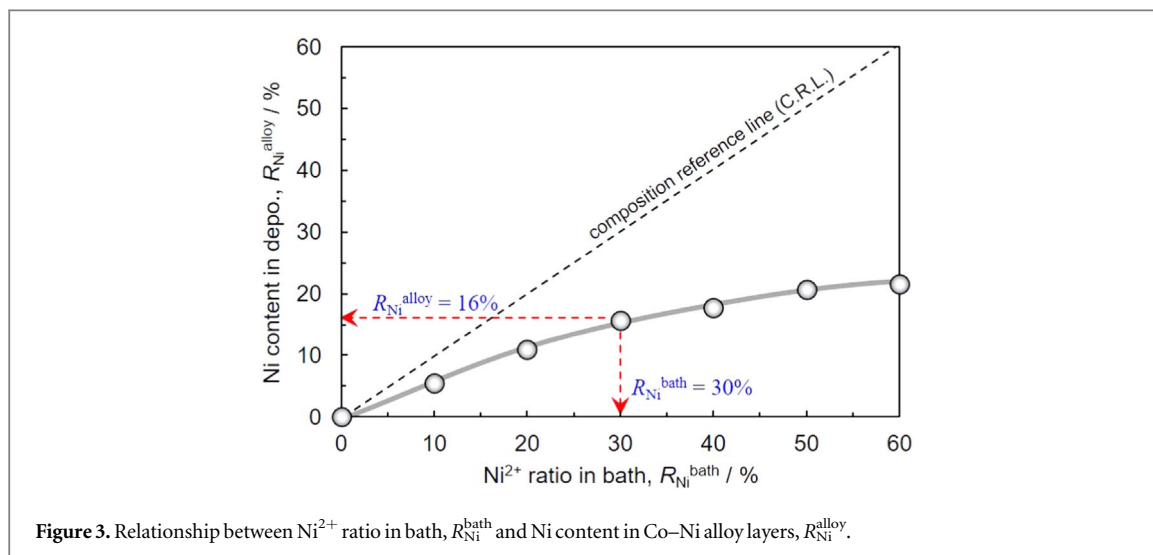
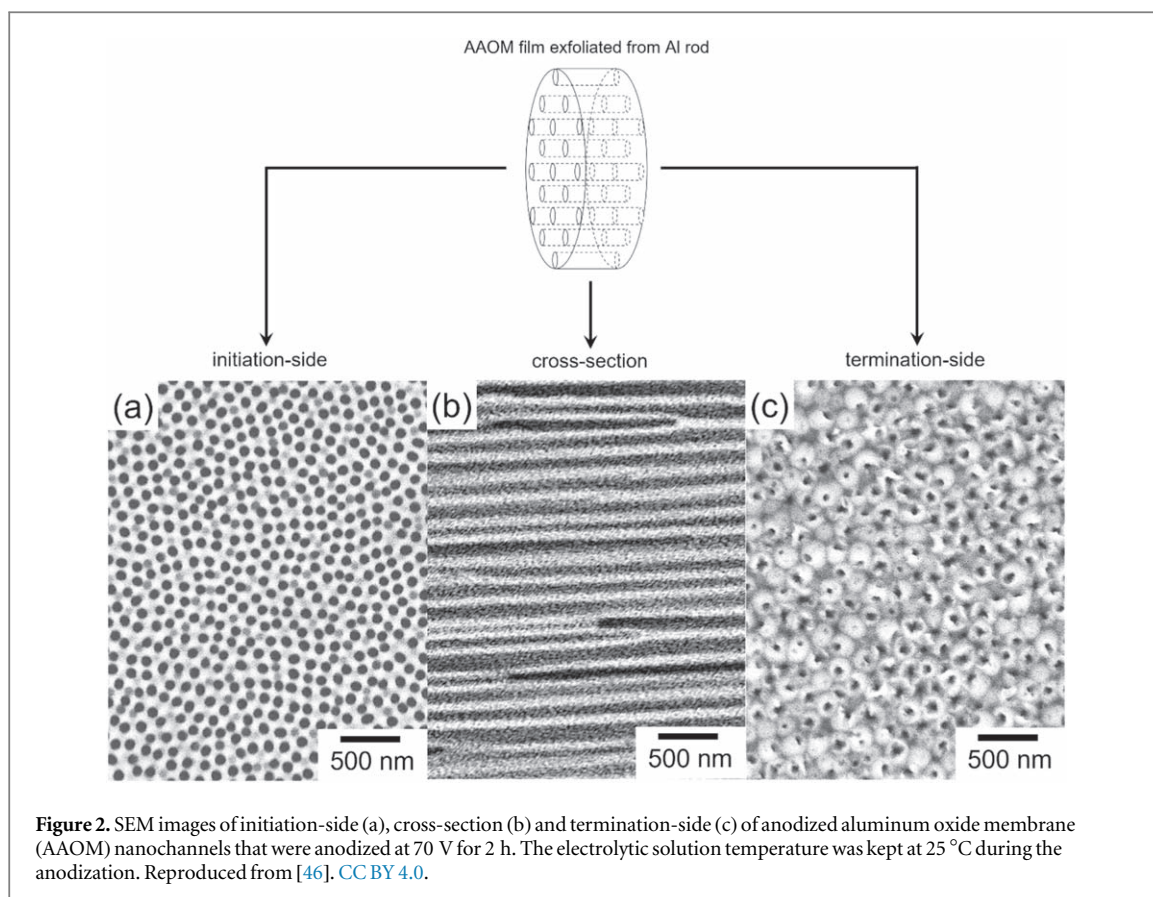
Figure 1 depicts a Co–Ni equilibrium phase diagram [22]. Co and Ni will form a solid solution in the  $\alpha$  (fcc) phase at the temperature range between the solidus and allotropic transformation (fcc- $\alpha$  phase to hcp- $\epsilon$  phase). Especially, at room temperature region, in the Ni content,  $x_{Ni}$  range more than  $\sim 35\%$ ,  $\alpha$  phase will be stabler than  $\epsilon$  phase. On the other hand, in the  $x_{Ni}$  range less than  $\sim 25\%$ ,  $\epsilon$  phase will be stabler than  $\alpha$  phase at room temperature region. It is well known that the magneto-crystalline anisotropy energy of  $\epsilon$  phase (hcp-Co:  $+4.1 \times 10^5 \text{ J m}^{-3}$ ) is quite larger than that of  $\alpha$  phase (fcc-Ni:  $-4.0 \times 10^4 \text{ J m}^{-3}$ ) [23]. Cobalt alloys with  $\epsilon$  (hcp) phase will be magnetized spontaneously along the  $c$ -axis direction which corresponds to the normal direction of (002) crystal plane. If Co–Ni/Cu multilayered nanocylinders with (002) preferential orientation in hcp Co–Ni alloy layers can be synthesized by using a pulsed potential electrodeposition technique into AAOM nanochannels, A novel CPP-GMR sensor with an excellent magnetoresistance and corrosion-resistance will be realized.

## 3. Results and discussion

### 3.1. Fabrication of anodized aluminum oxide membrane (AAOM) nanochannels

SEM images of initiation-side (figure 2(a)), cross-section (figure 2(b)), and termination-side (figure 2(c)) of an AAOM template which was anodized by applying 70 V for 2 h are shown in figure 2. As depicted in figure 2, the AAOM template owned a perfect nanochannel configuration with cylindrical pores. The average nanochannel diameter  $D$  and the inter-nanochannel distance  $D_{int}$  of the AAOM template were  $\sim 67 \text{ nm}$  and  $167 \text{ nm}$ , respectively, while the AAOM nanochannel length  $L$  was  $\sim 70 \mu\text{m}$ . Aspect ratio ( $L/D$ ) of the AAOM nanochannels was  $\sim 1,045$ . Ebihara, *et al* reported that inter-nanochannel distance  $D_{int}$  depended on the anodization voltage  $V_a$  even if the following parameters such as bath composition, temperature, and current density during the anodization were altered [24]. They discovered that  $D_{int}$  had a linear relationship with  $V_a$  if  $V_a$  is greater than 20 V as shown in the following equation (2).

$$D_{int} = 2.81V_a - 1.70 \quad (2)$$



According to equation (2),  $D_{\text{int}}$  can be estimated to be 195 nm if  $V_a$  is 70 V. Hence, the inter-nanochannel distance (167 nm), which was obtained in our experiment, was a little smaller than that (195 nm) in their study.

### 3.2. Electrochemical growth of Co–Ni/Cu multilayered nanocylinders

Figure 3 depicts the relationship between  $\text{Ni}^{2+}$  ratio in bath,  $R_{\text{Ni}}^{\text{bath}}$  and Ni content in Co–Ni alloy layers,  $R_{\text{Ni}}^{\text{alloy}}$ . With increasing  $R_{\text{Ni}}^{\text{bath}}$  up to 60%,  $R_{\text{Ni}}^{\text{alloy}}$  reached  $\sim 22\%$ , which is smaller than that in the composition reference line (C.R.L.) as shown in figure 3. It is well known that the abnormal co-electrodeposition behavior is occurred in Co–Ni alloy system [25]. In the abnormal co-electrodeposition behavior, less-noble  $\text{Co}^{2+}$  ions electrodeposit preferentially rather than  $\text{Ni}^{2+}$  ions. In the present study,  $R_{\text{Ni}}^{\text{alloy}}$  were smaller than that in the C.R.L. over the wide range of  $R_{\text{Ni}}^{\text{bath}}$  within 60% as described in figure 3.

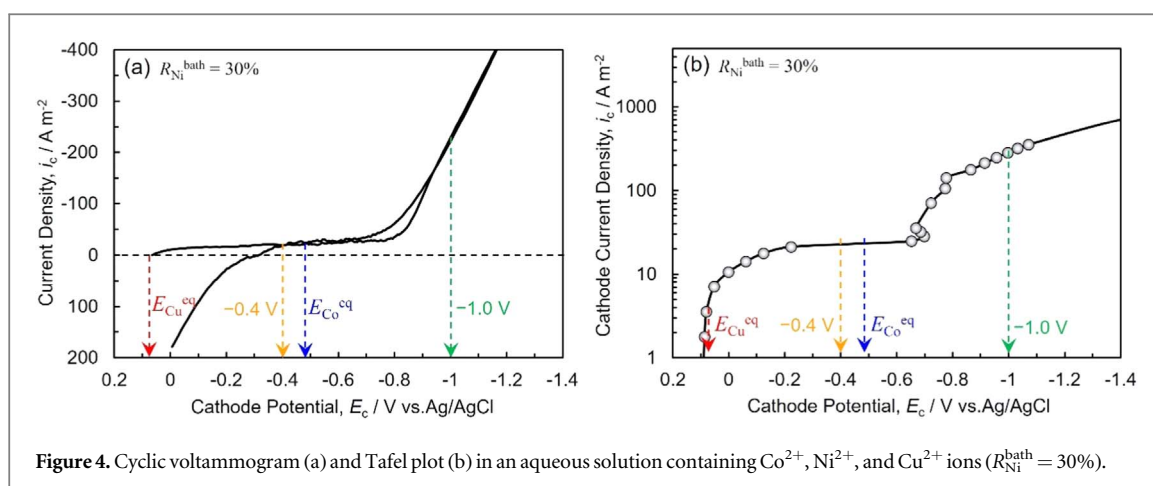


Figure 4. Cyclic voltammogram (a) and Tafel plot (b) in an aqueous solution containing  $Co^{2+}$ ,  $Ni^{2+}$ , and  $Cu^{2+}$  ions ( $R_{Ni}^{bath} = 30\%$ ).

A cyclic voltammogram (figure 4(a)) and the Tafel plot (figure 4(b)) to determine the optimum cathode potential range in an aqueous solution ( $R_{Ni}^{bath} = 30\%$ ) containing  $Cu^{2+}$  (0.005 M),  $Co^{2+}$  (0.35 M) and  $Ni^{2+}$  ions (0.15 M) are shown in figure 4. With shifting the cathode potential to the less-noble region, the cathodic current  $I_c$  drastically increased at the potential  $E_c$  of around +0.08 V. Utilizing the  $Cu^{2+}$  ions concentration and electrolytic solutions temperature, the electrochemical equilibrium potential of  $Cu/Cu^{2+}$  ( $E_{Cu}^{eq}$ ) should be calculated as around +0.07 V according to the following Nernst equation (3).

$$E^{eq} = E^0 + \frac{RT}{nF} \ln \frac{[M^{n+}]}{[M^0]} \quad (3)$$

Here,  $E_{Cu}^0$  (normal electrode potential of  $Cu/Cu^{2+}$ ) is 0.141 V.  $R$  (gas constant) is  $8.3 J K^{-1} mol^{-1}$ .  $T$  (solution temperature) is 313 K.  $n$  (valence of  $Cu^{2+}$  ions) is 2.  $F$  (Faraday constant) is  $96485 C mol^{-1}$ .  $[M^{n+}]/[M^0]$  corresponds to 0.005. As described above,  $I_c$  started to increase at  $E_c$  of around +0.08 V. This experimental value ( $E_c = +0.08$  V) is almost identical to the Nernst estimation value ( $E_{Cu}^{eq} = +0.07$  V). Therefore, the rising in  $I_c$  at  $E_c$  of around +0.08 V should be induced from the electrodeposition of  $Cu^{2+}$  ions. At  $I_c$  of  $\sim 20 A m^{-2}$ ,  $E_c$  shifted drastically from -0.2 to -0.7 V. In the current work, the  $Cu^{2+}$  ions concentration (0.005 M) was quite smaller than that of the total amount of  $Co^{2+}$  and  $Ni^{2+}$  ions (0.5 M). Therefore, the diffusion limitation of  $Cu^{2+}$  ions should be achieved at such a small  $I_c$  ( $\sim 20 A m^{-2}$ ). This diffusion limitation of the  $Cu^{2+}$  ions could result in the significant potential shift at  $I_c$  of  $\sim 20 A m^{-2}$ . On the contrary,  $I_c$  increased once more at  $E_c$  of around -0.7 V. According to the equation (3), the electrochemical equilibrium potentials of  $Co/Co^{2+}$  ( $E_{Co}^{eq}$ ) and  $Ni/Ni^{2+}$  ( $E_{Ni}^{eq}$ ) should be determined to around -0.490 V and -0.482 V, respectively. In this calculation, the standard electrode potential of  $Co/Co^{2+}$   $E_{Co}^0$  and  $Ni/Ni^{2+}$   $E_{Ni}^0$  are assumed to be -0.476 V and -0.456 V, respectively. Furthermore, regarding the concentration of  $Co^{2+}$  and  $Ni^{3+}$  ions,  $[Co^{2+}]/[Co^0]$  and  $[Ni^{2+}]/[Ni^0]$  are assumed to be 0.35 and 0.15, respectively. It is well recognized that the electrodeposition of iron-group metals (M: Fe, Co, Ni) accompanies a significant overpotential owing to a rate-determining reduction steps by means of  $M(OH)^+$  ions (Bockris mechanism) [26]. Hence, the increase in  $I_c$  at  $E_c$  of around -0.7 V should be induced by the electrodeposition of  $Co^{2+}$  and  $Ni^{2+}$  ions [27]. On the contrary, when  $E_c$  was scanned from -1.2 V to an electrochemical noble region, an anodic current was detected in the potential region from -0.3 to 0 V (figure 4(a)). Since the potential region (from -0.3 to 0 V) is quite nobler than the electrochemical equilibrium potentials of  $Co/Co^{2+}$  and  $Ni/Ni^{2+}$ , this anodic current should be induced from the dissolution of electrodeposited Co-Ni alloys. Because of the reason given, the most recommendable cathode potentials for electrodepositing Cu and Co-Ni alloy layers were decided to be around -0.40 V and -1.00 V, respectively, to make Co-Ni/Cu multilayered nanocylinder arrays.

Figure 5 depicts the waveform of pulsed potential  $E_c$  (a), response current (for initial time)  $I_c$  (b) and response current (for all time)  $I_c$  (c) during the electrochemical growth of  $Co_{84}Ni_{16}/Cu$  multilayered nanocylinders in an aqueous solution ( $R_{Ni}^{bath} = 30\%$ ) containing  $Cu^{2+}$  (0.005 M),  $Co^{2+}$  (0.35 M) and  $Ni^{2+}$  ions (0.15 M). The nobler cathode potential (-0.4 V) was applied for 1.0 s to while the less-nobler cathode potential (-1.0 V) was utilized for 0.1 s. As shown in Tafel plot (figure 4(b)), Co-Ni alloy layers will be deposited at -1.0 V while Cu layers will be deposited at -0.4 V.

Based on the electrodeposition time for filling up the AAOM nanochannels as depicted in figure 5(c), the bilayer thickness of Co-Ni/Cu,  $t_{CoNi/Cu}$  can be calculated by utilizing the following equation (4).

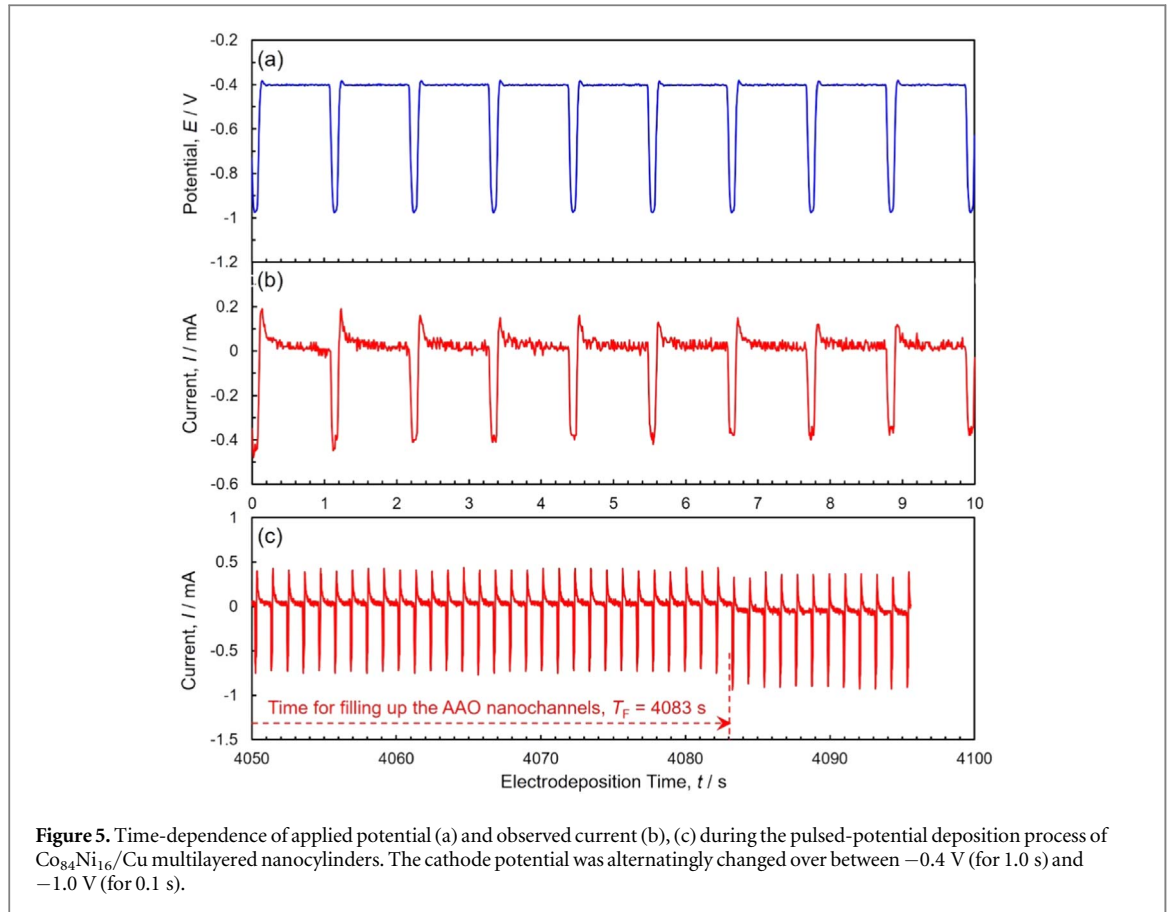


**Figure 5.** Time-dependence of applied potential (a) and observed current (b), (c) during the pulsed-potential deposition process of  $\text{Co}_{84}\text{Ni}_{16}/\text{Cu}$  multilayered nanocylinders. The cathode potential was alternately changed over between  $-0.4$  V (for 1.0 s) and  $-1.0$  V (for 0.1 s).

$$t_{\text{CoNi/Cu}} = L \frac{T_{\text{CoNi}} + T_{\text{Cu}}}{T_F} \quad (4)$$

In this equation,  $L$  means the average nanochannel length while  $T_F$ ,  $T_{\text{CoNi}}$  and  $T_{\text{Cu}}$  are the nanochannel filling up time, the deposition time in a pulse for Co–Ni alloy and Cu layer, respectively. For instance, as depicted in figure 5(c),  $L$ ,  $T_F$ ,  $T_{\text{CoNi}}$  and  $T_{\text{Cu}}$  were  $70 \mu\text{m}$ , 4083 s, 0.1 s and 1.0 s, respectively. Hence, according to the equation (4),  $t_{\text{CoNi/Cu}}$  can be determined to  $\sim 18.9$  nm.

By using an EDX analyzer, the composition of Co–Ni alloy ( $X_{\text{CoNi}}$ ) and that of Cu ( $X_{\text{Cu}}$ ) in the multilayered nanocylinders were decided to 63.4% and 36.6%, respectively. Hence, each Co–Ni alloy layer ( $t_{\text{CoNi}}$ ) and Cu layer thickness ( $t_{\text{Cu}}$ ) can be calculated from the equations (5) and (6), respectively.

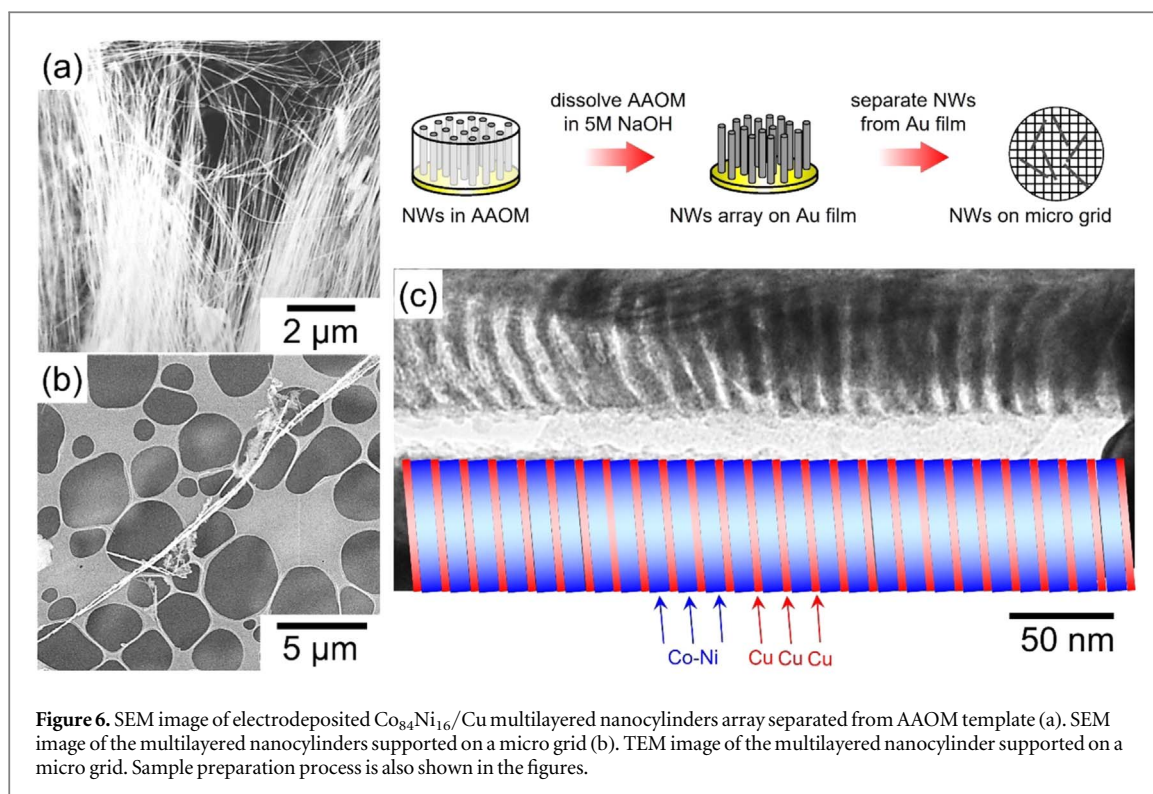
$$t_{\text{CoNi}} = t_{\text{CoNi/Cu}} \frac{X_{\text{CoNi}}}{100} \quad (5)$$

$$t_{\text{Cu}} = t_{\text{CoNi/Cu}} \frac{X_{\text{Cu}}}{100} \quad (6)$$

According to the equations (5) and (6),  $t_{\text{CoNi}}$  and  $t_{\text{Cu}}$  were determined to  $\sim 12.0$  nm and  $\sim 6.9$  nm, respectively. Tang *et al* reported that the CPP-GMR effect of Co–Ni/Cu nanocylinders with alternating Co–Ni alloy layer (10.2 nm) and Cu layer (4.2 nm) achieved up to  $\sim 23\%$  [14]. Therefore, the  $t_{\text{Cu}}$  which was obtained in our study ( $\sim 6.9$  nm) was slightly thicker than that was reported in their work (4.2 nm). Likewise,  $t_{\text{CoNi}}$  which was determined in our study ( $\sim 12.0$  nm) was also slightly thicker than that was reported in their work (10.2 nm).

### 3.3. Alternating structure of electrochemically fabricated Co–Ni/Cu nanocylinders

Figures 6(a) and (b) depicts the SEM image of electrodeposited  $\text{Co}_{84}\text{Ni}_{16}/\text{Cu}$  multilayered nanocylinders array separated from AAOM template (figure 6(a)) and that of the multilayered nanocylinders supported on a micro grid (figure 6(b)), respectively. TEM image of the multilayered nanocylinder supported on a micro grid is shown in figure 6(c). The sample preparation process is also shown in figure 6. Following the electrodeposition of  $\text{Co}_{84}\text{Ni}_{16}/\text{Cu}$  multilayered nanocylinders, the AAOM templates were dissolved in 5 M NaOH aqueous solution. Then, the nanocylinders array sample was rinsed in pure water to remove the alkaline solution. After that, the nanocylinders were separated from a gold film in the pure water with ultrasonic irradiation. The dispersed nanocylinders in the pure water were gathered by applying a magnetic field. The dense nanocylinders in the pure water were sucked into a Pasteur pipette and ejected on a micro-grid for TEM observation. As shown in



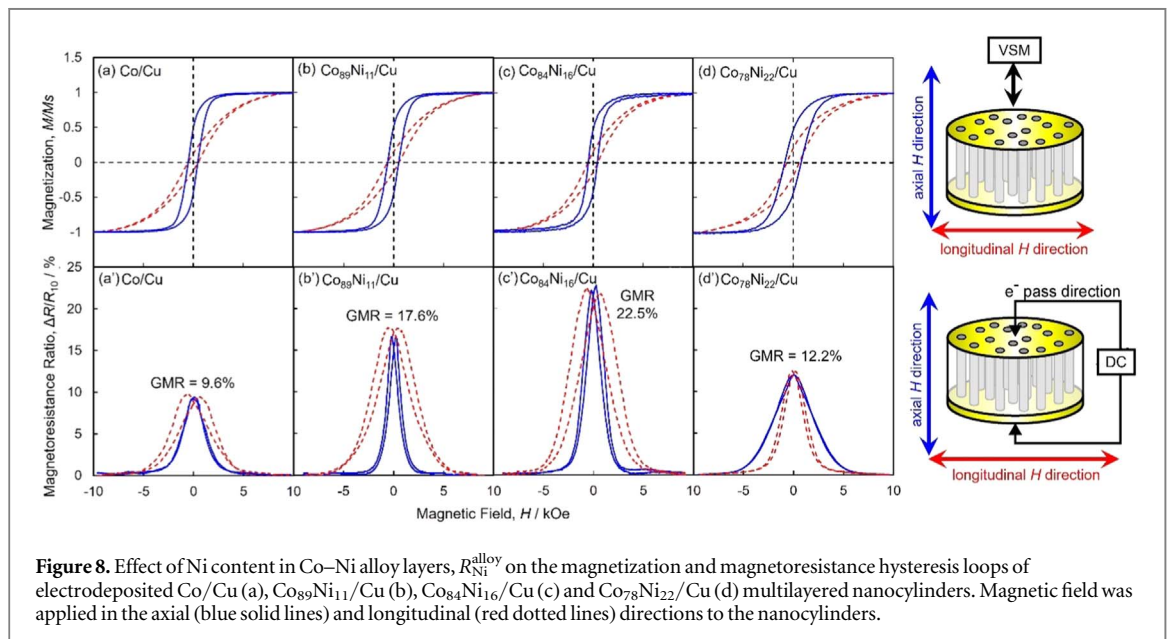
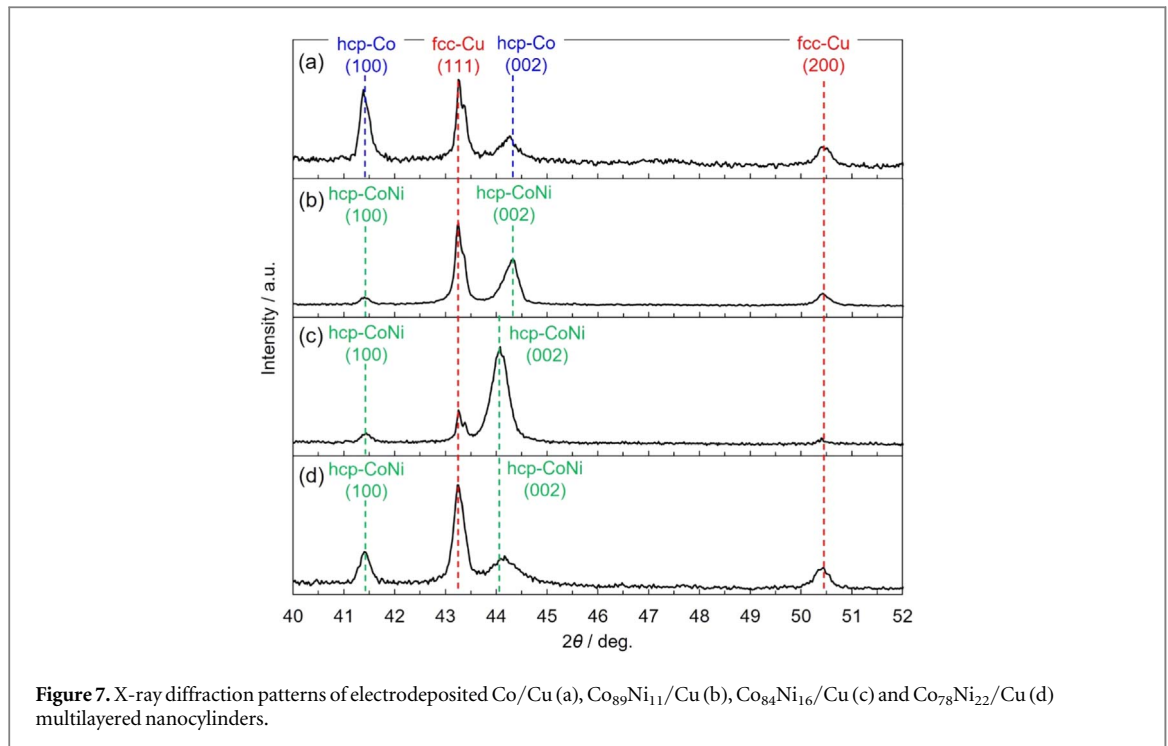
**Figure 6.** SEM image of electrodeposited  $\text{Co}_{84}\text{Ni}_{16}/\text{Cu}$  multilayered nanocylinders array separated from AAOM template (a). SEM image of the multilayered nanocylinders supported on a micro grid (b). TEM image of the multilayered nanocylinder supported on a micro grid. Sample preparation process is also shown in the figures.

figure 6(a), it was revealed that the numerous nanocylinders were arranged in an array structure which was originated from the AAOM nanochannel structure. It was also obvious that the axial length of nanocylinders with an ultra-large aspect ratio reached up more than  $30\ \mu\text{m}$  as shown in figure 6(b). The Co–Ni/Cu alternating structure was also obvious as depicted in figure 6(c) and the diameter  $D$  was determined to be  $\sim 63\ \text{nm}$ . In a bright-field TEM image, it is well-known that the ferromagnetic layers appear darker than the non-magnetic layers [28]. Hence, the dark and bright-colored layers seem to correspond to ferromagnetic Co–Ni alloy and non-magnetic Cu phases, respectively. The average layer thickness of Co–Ni alloy and Cu layers are determined to be  $\sim 9.6\ \text{nm}$  and  $\sim 3.8\ \text{nm}$ , respectively. These layer thickness values were almost identical to those ( $\sim 10.2\ \text{nm}$  and  $\sim 4.2\ \text{nm}$ ) which were reported by Tang *et al* [14].

Figure 7 shows the XRD profiles of electrochemically fabricated Co/Cu (a),  $\text{Co}_{89}\text{Ni}_{11}/\text{Cu}$  (b),  $\text{Co}_{84}\text{Ni}_{16}/\text{Cu}$  (c) and  $\text{Co}_{78}\text{Ni}_{22}/\text{Cu}$  (d) multilayered nanocylinders. The diffraction peaks that correspond to hcp-Co, hcp-CoNi, and fcc-Cu phases were detected as shown in figure 7. In the diffraction pattern of Co/Cu multilayered nanocylinders (figure 7(a)), it was obvious that hcp-Co (1 0 0) was orientated preferentially. Based on our former report on the Pangarov's two-dimensional nucleation theory, preferential crystal orientation of electrodeposited cobalt strongly depended on the cathode potential during the electrodeposition process [29, 30]. If the cathode potential range was controlled to be less-nobler value than  $-0.77\ \text{V}$ , hcp-Co (1 0 0) was preferentially orientated while hcp-Co (0 0 2) preferentially orientated if the potential range was set to be nobler than  $-0.77\ \text{V}$ . In this current work, the cathode potential for growing Co layers  $E_C$  was adjusted to  $-1.0\ \text{V}$ . Hence, hcp-Co (1 0 0) should be orientated preferentially according to the Pangarov's theory. On the other hand, in the  $\text{Co}_{89}\text{Ni}_{11}/\text{Cu}$  (figure 7(b)) and  $\text{Co}_{84}\text{Ni}_{16}/\text{Cu}$  (figure 7(c)) multilayered nanocylinders, hcp-CoNi (0 0 2) was preferentially orientated. Based on our former report, hcp-Co nanocylinders array with (0 0 2) preferential orientation exhibited an uniaxial magnetization behavior along to the nanocylinders long axis direction [30]. Therefore, hcp-CoNi (0 0 2) should be preferentially orientated if Co–Ni/Cu multilayered nanocylinders with a long axial length induces the uniaxial magnetization behavior to the long axis direction. On the contrary, in the XRD profile (figure 7(d)) which was obtained from the  $\text{Co}_{78}\text{Ni}_{22}/\text{Cu}$  multilayered nanocylinders, both diffraction peaks of hcp-CoNi (1 0 0) and (0 0 2) were detected. With increasing Ni content in the Co-alloy layers, saturation magnetic moment  $M_s$  will be decreased because  $M_s$  of pure Ni is smaller than that of pure Co. Hence, the preferential orientation of hcp-CoNi (0 0 2) will be disappeared by decreasing the spontaneous magnetization effect due to an increase in Ni content in the Co-alloy layers.

### 3.4. Magnetoresistance behavior of electrodeposited Co–Ni/Cu multilayered nanocylinders

Magnetic hysteresis loops of electrodeposited Co/Cu (a),  $\text{Co}_{89}\text{Ni}_{11}/\text{Cu}$  (b),  $\text{Co}_{84}\text{Ni}_{16}/\text{Cu}$  (c) and  $\text{Co}_{78}\text{Ni}_{22}/\text{Cu}$  (d) multilayered nanocylinders are shown in figures 8(a)–(d). The samples were magnetized in the axial (solid



blue lines) and longitudinal (dotted red lines) directions to the nanocylinders. As depicted in figures 8(a)–(d), the multilayered nanocylinders reached the saturation magnetization at the saturation field,  $H_{sat} \sim 2.5$  kOe with the axial direction magnetic field (blue solid lines). On the other hand, the saturation magnetization was achieved at the saturation field,  $H_{sat} \sim 5$  kOe with the longitudinal direction magnetic field (red dotted lines). Hence, it was revealed that the multilayered nanocylinders were magnetized spontaneously to the axial direction. This magnetization behavior of the multilayered nanocylinders is quite similar to that of the homogeneous pure metal or alloy nanocylinders [31–34]. It is well known that the magnetic nanocylinder arrays are magnetized spontaneously along the long axis direction [35–38]. Reddy *et al* reported that Fe–Ga/Cu multilayered nanocylinders with the diameter of  $\sim 100$  nm was fabricated utilizing a pulsed current deposition process into a commercially available AAOM film [39]. They revealed that the multilayered nanocylinders with each layer thickness of  $\sim 100$  nm were magnetized easily along to the axial direction and reached the saturation magnetization at the saturation field,  $H_{sat} \sim 2.5$  kOe. This magnetization performance which was observed in Fe–Ga/Cu nanocylinders quite resembles the results observed in our current study (Co–Ni/Cu nanocylinders). Therefore, the uniaxial magnetization behavior as shown in figures 8 (a)–(d) could be interpreted by the

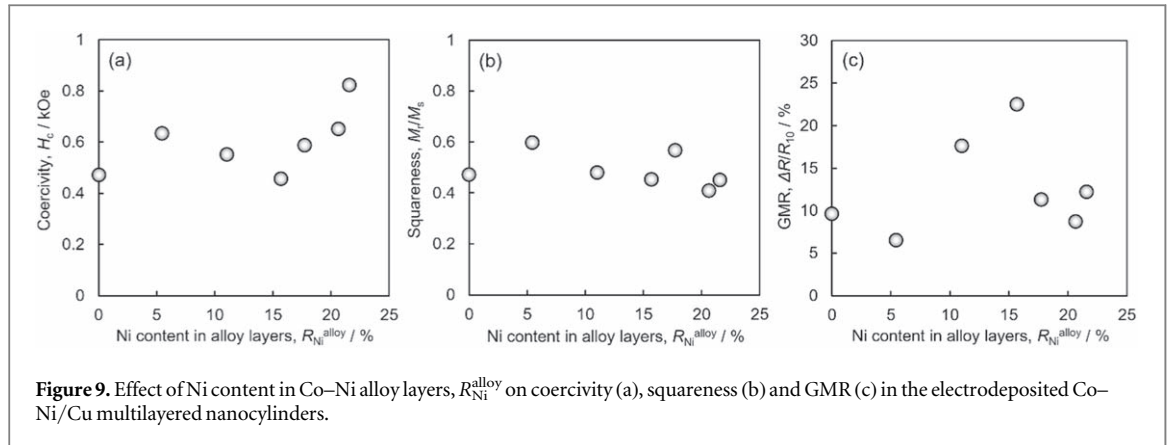


**Figure 9.** Effect of Ni content in Co–Ni alloy layers,  $R_{Ni}^{alloy}$  on coercivity (a), squareness (b) and GMR (c) in the electrodeposited Co–Ni/Cu multilayered nanocylinders.

magnetic dipole-dipole interaction between Co–Ni alloy layers that are separated by means of a Cu layer. Tang *et al* reported that the effect of dipole-dipole interactions between  $Co_{56}Ni_{44}$  alloy layers ( $t_{CoNi} = 10.2$  nm) which were separated by Cu layers ( $t_{Cu} = 4.2$  nm, 8.4 nm, 12.6 nm, 21 nm and 42 nm) on the CPP-GMR performance of Co–Ni/Cu multilayered nanocylinders [14]. They revealed that the saturation field,  $H_{sat}$  of Co–Ni/Cu multilayered nanocylinders tended to decrease with increasing  $t_{Cu}$  due to decreasing the dipole-dipole interaction between the adjacent Co–Ni alloy layers. On the contrary, the saturation field,  $H_{sat}$  was increased with decreasing  $t_{Cu}$  due to the dipolar interlayer coupling which tended to align the magnetizations of adjacent Co–Ni alloy layers antiparallel to each other. This antiparallel alignment will enhance the CPP-GMR performance. Also, the dipolar interlayer coupling will induce the decreasing coercivity and squareness in the magnetization performance. According to their study,  $H_{sat}$  of Co–Ni/Cu multilayered nanocylinders with  $t_{Cu}$  of 4.2 nm was  $\sim 3.5$  kOe in the longitudinal direction to the nanocylinders. In the present study,  $H_{sat}$  of Co–Ni/Cu multilayered nanocylinders with  $t_{Cu}$  was 3.8 nm was  $\sim 5$  kOe which was larger than the value reported by Tang *et al* [14]. This difference seems to be owing to the difference of diameter in each nanocylinder. The diameter was  $\sim 67$  nm in the present study while that was  $\sim 250$  nm in the report Tang *et al* [14]. Demagnetization field in the longitudinal direction to the nanocylinders will be enhanced by decreasing the diameter of nanocylinders. Hence,  $H_{sat}$  in the present study was larger than the value reported by Tang *et al* [14].

Figures 8 (a')–(d') shows the magnetoresistance (MR) hysteresis loops of electrodeposited Co/Cu (a'),  $Co_{89}Ni_{11}/Cu$  (b'),  $Co_{84}Ni_{16}/Cu$  (c') and  $Co_{78}Ni_{22}/Cu$  (d') multilayered nanocylinders. The samples were magnetized in the axial (solid blue lines) and longitudinal (dotted red lines) directions to the nanocylinders. The MR ratio,  $\Delta R/R_{10}$ , was defined as the following equation (7).

$$\frac{\Delta R}{R_{10}}(\%) = \frac{R_x - R_{10}}{R_{10}} \times 100 \quad (7)$$

In this equation,  $R_{10}$  indicates the resistance of nanocylinders which was obtained at 10 kOe. On the contrary,  $R_x$  means the resistance of nanocylinders which was measured at the applied magnetic field less than 10 kOe.

As depicted in figures 8 (a')–(d'), with increasing the applied magnetic field  $H$  in the axial direction (solid blue lines), the magnetoresistance ratio  $\Delta R/R_{10}$  quickly decreased and reached almost zero at the magnetic field range from 2.5 to 5 kOe. On the contrary, with increasing  $H$  in the longitudinal direction (red dotted lines),  $\Delta R/R_{10}$  slowly decreased and reached around zero at the magnetic of  $\sim 5$  kOe. This tendency shows good agreement with the magnetization behavior of the multilayered nanocylinders which was shown in figures 8 (a)–(d). These anisotropic performance in the magnetoresistance hysteresis loops corresponds well to the results which were studied by the other investigators [40].

Figure 9 depicts the effect of Ni content in Co–Ni alloy layers,  $R_{Ni}^{alloy}$  on coercivity,  $H_c$  (a), squareness,  $M_r/M_s$  (b) and GMR,  $\Delta R/R_{10}$  (c) in the Co–Ni/Cu multilayered nanocylinders. These data were obtained when the samples were magnetized in the long axis direction to the nanocylinders. As depicted in figures 9(a) and (b),  $H_c$  was minimum ( $\sim 0.46$  kOe) at  $R_{Ni}^{alloy}$  of  $\sim 16\%$  while  $M_r/M_s$  was almost constant value of  $\sim 0.5$  over the whole range of  $R_{Ni}^{alloy}$ . Takahashi *et al* reported that the magnetic anisotropy of Co–Ni alloys strongly depends on the Ni content [41]. They revealed that uniaxial magnetic anisotropy  $K_u$  for Co–Ni alloys shifted from negative to positive value with increasing the Ni content up to 20%. Based on their report,  $K_u$  for Co and Co–20%Ni alloy were  $-5 \times 10^5$  and  $+4 \times 10^5$  erg  $cm^{-3}$ , respectively, whereas  $K_u$  for Co–10%Ni alloy was almost zero. Anisotropic magnetic field  $H_k$  of ferromagnetic alloys decreases with decreasing the uniaxial magnetic anisotropy  $K_u$  as shown in the following equation (8).

**Table 1.** Summary of CPP-GMR performance (at room temperature) of multilayered nanocylinders electrodeposited into AAO that were reported by the other researchers. The nanocylinders in [4, 5] were electrodeposited into ion-track-etched polycarbonate membranes.

Authors	FM/NM	GMR/%	D/nm	L/ $\mu$ m	L/D	$t_{\text{Co}}$ /nm	$t_{\text{Cu}}$ /nm	Year	References
Piroux <i>et al</i>	Co/Cu	15	40	10	250	10	10	1994	[4]
Blondel <i>et al</i>	Co/Cu	14	80	6	75	5	5	1994	[5]
Evans <i>et al</i>	CoNi/Cu	55	300	60	200	5	2	2000	[13]
Ohgai <i>et al</i>	Co/Cu	15	60	2	33	10	10	2004	[8]
Tang <i>et al</i>	Co/Cu	14	300	60	200	8	10	2006	[9]
Tang <i>et al</i>	CoNi/Cu	23	300	60	200	10	4	2007	[14]
Davis <i>et al</i>	CoNiFe/Cu	20	190	60	316	5.6	4.2	2010	[15]
Shakya <i>et al</i>	FeCoNi/Cu	15	300	60	200	14	10	2012	[43]
Cox <i>et al</i>	FeCoNi/Cu	14	200	10–20	50–100	25	8	2013	[44]
Han <i>et al</i>	Co/Cu	13	50	11	220	50	5	2016	[45]
Kamimura <i>et al</i>	Co/Cu	24	75	70	933	19	1.4	2020	[21]
Mizoguchi <i>et al</i>	Co/Cu	23	50	60	1200	8.6	4	2021	[46]
Ide <i>et al</i>	Co/Cu	32	60	60	1000	7	2.4	2021	[47]
Fan <i>et al</i>	Co/Cu	27	30–100	7	70–235	32	15	2022	[48]

$$H_k = \frac{2K_u}{M_s} \quad (8)$$

Here,  $M_s$  is the saturation magnetization. If the sample is a single domain particle, the magnetization reversal process will proceed by a coherent rotation mode according to Stoner-Wohlfarth model. In this magnetization process,  $H_c$  will be identical to  $H_k$ . However, if the sample is composed of a multi-domain structure, the magnetization reversal process will proceed by a domain wall movement mode. In this magnetization process,  $H_c$  will be smaller than  $H_k$  because the crystal defects such as grain boundaries and dislocations will reduce the anisotropic magnetic field. Kronmüller reported the relationship between  $H_c$  and  $H_k$  as the following equation (9) [42].

$$H_c = \alpha H_k - NM_s \quad (9)$$

Here,  $\alpha$  is the reduction parameter in the anisotropic magnetic field due to the crystal defects on grain boundaries.  $N$  is the demagnetization factor which is related to the local demagnetization field. Hence, in the present study, the minimum coercivity  $H_c$  at  $R_{\text{Ni}}^{\text{alloy}}$  of  $\sim 16\%$  should be induced from decreasing the uniaxial magnetic anisotropy  $K_u$ . Further, as depicted in figure 9(c),  $\Delta R/R_{10}$  was achieved up to 22.5% at  $R_{\text{Ni}}^{\text{alloy}}$  of  $\sim 16\%$ . Shakya *et al* found that the GMR of electrodeposited FeCoNi/Cu multilayered nanocylinders was affected by the coercivity [43]. They found that the GMR of FeCoNi/Cu multilayered nanocylinders increased up to 14.56% with decreasing the coercivity  $H_c$  down to 0.0086 T ( $\sim 0.086$  kOe). Therefore, in our study, the maximum GMR (22.5%) at  $R_{\text{Ni}}^{\text{alloy}}$  of  $\sim 16\%$  could be achieved by decreasing the coercivity  $H_c$  and the uniaxial magnetic anisotropy  $K_u$ . Table 1 shows the summary of CPP-GMR performances (at room temperature) of electrodeposited multilayered nanocylinders that were reported by the other researchers. Most researchers have reported that the CPP-GMR value reached up to around 15 ~ 20% at room temperature in the  $t_{\text{Co}}$  range from 5 to 20 nm and the  $t_{\text{Cu}}$  range from 5 to 10 nm. Those values give good agreement with the value obtained in the present study ( $t_{\text{CoNi}}$ : 9.6 nm,  $t_{\text{Cu}}$ : 3.8 nm).

## 4. Conclusion

By applying a pulsed current electrodeposition method, Co–Ni/Cu multilayered nanocylinders with a large aspect ratio  $L/D$  of  $\sim 1,045$  ( $D$  of  $\sim 67$  nm and  $L$  of  $\sim 70$   $\mu$ m) were electrochemically fabricated in AAOM nanochannels. The layer-by-layer structure with alternating  $\text{Co}_{84}\text{Ni}_{16}$  alloy layer (thickness of  $\sim 9.6$  nm) and Cu layer (thickness of  $\sim 3.8$  nm) was confirmed by TEM observation and x-ray diffraction patterns. The multilayered nanocylinders were magnetized spontaneously in the long axis direction which corresponds to the perpendicular direction to the interfaces of the multilayers. The minimum coercivity of  $\sim 0.46$  kOe was achieved in  $\text{Co}_{84}\text{Ni}_{16}/\text{Cu}$  multilayered nanocylinders. The maximum CPP-GMR was achieved up to 22.5% at room temperature in  $\text{Co}_{84}\text{Ni}_{16}/\text{Cu}$  multilayered nanocylinders.

## Acknowledgments

The authors thank Japan Society for the Promotion of Science (JSPS: 18H01754) for the financial support.

## Data availability statement

The data that support the findings of this study are available upon reasonable request from the authors.

## Competing interests

The authors declare that they have no competing interests.

## Authors' contributions

K.N carried out experiments, analyzed data, and wrote manuscript. M.H. carried out experiments and analyzed data. T.O. designed the study, supervised the project, and analyzed data. All authors read and approved the final manuscript.

## ORCID iDs

Takeshi Ohgai  <https://orcid.org/0000-0001-6872-7888>

## References

- [1] Chappert C, Fert A and Van Dou FN 2007 The emergence of spin electronics in data storage *Nat. Mater.* **6** 813–23
- [2] Baibich M N, Broto J M, Fert A, Nguyen V D F and Petroff F 1988 Giant magnetoresistance of (001)Fe/(001)Cr magnetic super-lattices *Phys. Rev. Lett.* **61** 2472–5
- [3] Binasch G, Grünberg P, Saurenbach F and Zinn W 1989 Enhanced magnetoresistance in Fe-Cr layered structures with antiferromagnetic interlayer exchange *Phys. Rev. B* **39** 4828
- [4] Piroux L, George J M, Despres J F, Leroy C, Ferain E, Legras R, Ounadjela K and Fert A 1994 Giant magnetoresistance in magnetic multilayered nanowires *Appl. Phys. Lett.* **65** 2484
- [5] Blondel A, Meier J P, Doudin B and Ansermet J P 1994 Giant magnetoresistance of nanowires of multilayers *Appl. Phys. Lett.* **65** 3019
- [6] López Antón R, Andrés J P, Ipatov M, González J A, González J, Zhukova V and Zhukov A 2021 Magneto-transport properties of Co-Cu thin films obtained by co-sputtering and sputter gas aggregation *Nanomaterials* **11** 134
- [7] Liu K, Nagodawithana K, Searson P C and Chien C L 1995 Perpendicular giant magnetoresistance of multilayered Co/Cu nanowires *Phys. Rev. B* **51** 7381–4
- [8] Ohgai T, Hoffer X, Gravier L and Ansermet J P 2004 Electrochemical surface modification of aluminium sheets for application to nano-electronic devices: anodization aluminium and cobalt-copper electrodeposition *J. Appl. Electrochem.* **34** 1007–12
- [9] Tang X T, Wang G C and Shima M 2006 Perpendicular giant magnetoresistance of electrodeposited Co/Cu-multilayered nanowires in porous alumina templates *J. Appl. Phys.* **99** 033906
- [10] Pullini D, Busquets D, Ruotolo A, Innocenti G and Amigó V 2007 Insights into pulsed electrodeposition of GMR multilayered nanowires *J. Magn. Magn. Mater.* **316** e242–5
- [11] Cox B, Davis D and Crews N 2013 Creating magnetic field sensors from GMR nanowire networks *Sens. Actuat. A Phys.* **203** 335–40
- [12] Mapelli C, Casalino C, Strada A, Gruttadauria A, Barella S, Mombelli D, Longaretti E and Perego F 2020 Comparison of the combined oxidation and sulphidation behavior of nickel- and cobalt-based alloys at high temperature *J. Mater. Res. Technol.* **9** 15679–92
- [13] Evans P R, Yi G and Schwarzacher W 2000 Current perpendicular to plane giant magnetoresistance of multilayered nanowires electrodeposited in anodic aluminum oxide membranes *Appl. Phys. Lett.* **76** 481–3
- [14] Tang X T, Wang G C and Shima M 2007 Layer thickness dependence of CPP giant magnetoresistance in individual CoNi/Cu multilayer nanowire grown by electrodeposition *Phys. Rev. B* **75** 134404
- [15] Davis D, Zamanpour M, Moldovan M, Young D and Podlaha E J 2010 Electrodeposited, GMR CoNiFeCu nanowires and nanotubes from electrolytes maintained at different temperatures *J. Electrochem. Soc.* **157** D317–22
- [16] Masuda H and Fukuda K 1995 Ordered metal nanohole arrays made by a two-step replication of honeycomb structures of anodic alumina *Science* **268** 1466–8
- [17] Asoh H, Ono S, Hirose T, Nakao M and Masuda H 2003 Growth of anodic porous alumina with square cells *Electrochim. Acta* **48** 3171–4
- [18] Ohgai T, Mizumoto M, Nomura S and Kagawa A 2007 Electrochemical fabrication of metallic nanowires and metal oxide nanopores *Mater. Manuf. Process.* **22** 440–3
- [19] Agarwal S, Pohl D, Patra A K, Nielsch K and Khatri M S 2019 Preparation and nanoscale characterization of electrodeposited CoFe-Cu multilayer nanowires *Mater. Chem. Phys.* **230** 231–8
- [20] Neetzl C, Ohgai T, Yanai T, Nakano M and Fukunaga H 2017 Uniaxial magnetization performance of textured Fe nanowire arrays electrodeposited by a pulsed potential deposition technique *Nanoscale Res. Lett.* **12** 598
- [21] Kamimura H, Hayashida M and Ohgai T 2020 CPP-GMR performance of electrochemically synthesized Co/Cu multilayered nanowire arrays with extremely large aspect ratio *Nanomaterials* **10** 5
- [22] Nishizawa T and Ishida K 1983 The Co-Ni (Cobalt-Nickel) system *Bulletin of Alloy Phase Diagrams* **4** 390–5
- [23] Moskaltsova A, Proenca M P, Nedukh S V, Sousa C T, Vakula A, Kakazei G N, Tarapov S I and Araujo J P 2015 Study of magnetoelastic and magnetocrystalline anisotropies in  $\text{Co}_x\text{Ni}_{1-x}$  nanowire arrays *J. Magn. Magn. Mater.* **374** 663–8
- [24] Ebihara K, Takahashi H and Nagayama M 1983 Structure and density of anodic oxide films formed on aluminum in oxalic acid solutions *J. Met. Finish. Soc. Jpn.* **34** 548–53
- [25] Armanyanov S 2000 Crystallographic structure and magnetic properties of electrodeposited cobalt and cobalt alloys *Electrochim. Acta* **45** 3323–35

- [26] Bockris J O 'M and Kita H 1961 Analysis of Galvanostatic transients and application to the iron electrode reaction *J. Electrochem. Soc.* **108** 676–81
- [27] Ohgai T, Tanaka Y and Fujimaru T 2012 Soft magnetic properties of Ni–Cr and Co–Cr alloy thin films electrodeposited from aqueous solutions containing trivalent chromium ions and glycine *J. Appl. Electrochem.* **42** 893–9
- [28] Shirazi Tehrani A, Almasi Kashi M, Ramazani A and Montazer A H 2016 Axially adjustable magnetic properties in arrays of multilayered Ni/Cu nanowires with variable segment sizes *Superlattices Microstruct.* **95** 38–47
- [29] Pangarov N A and Vitkova S D 1966 Preferred orientation of electrodeposited cobalt crystallites *Electrochim. Acta* **11** 1733–45
- [30] Saeki R and Ohgai T 2018 Effect of growth rate on the crystal orientation and magnetization performance of cobalt nanocrystal arrays electrodeposited from aqueous solution *Nanomaterials* **8** 566
- [31] Whitney T M, Jiang J S, Seanson P C and Chien C L 1993 Fabrication and magnetic properties of arrays of metallic nanowires *Science* **261** 1316–9
- [32] Ferre R, Ounadjela K, George J M, Piroux L and Dubois S 1997 Magnetization processes in nickel and cobalt electrodeposited nanowires *Phys. Rev. B* **56** 14066–75
- [33] Li D, Thompson R S, Bergmann G and Lu J G 2008 Template-based synthesis and magnetic properties of cobalt nanotube arrays *Adv. Mater.* **20** 4575–8
- [34] Ohgai T, Washio R and Tanaka Y 2012 Anisotropic magnetization behavior of electrodeposited nanocrystalline Ni–Mo alloy thin films and nanowires array *J. Electrochem. Soc.* **159** H800–4
- [35] Metzger R M, Kononov V V, Sun M, Xu T, Zangari G, Xu B, Benakli M and Doyle W D 2000 Magnetic nanowires in hexagonally ordered pores of alumina *IEEE Trans. Mag.* **36** 30–5
- [36] Zeng H, Zheng M, Skomski R, Sellmyer D J, Liu Y, Menon L and Bandyopadhyay S 2000 Magnetic properties of self-assembled Co nanowires of varying length and diameter *J. Appl. Phys.* **87** 4718–20
- [37] Han X, Liu Q, Wang J, Li S, Ren Y, Liu R and Li F 2009 Influence of crystal orientation on magnetic properties of hcp Co nanowire arrays *J. Phys. D: Appl. Phys.* **42** 095005
- [38] Ohgai T, Fujimaru T and Tanaka Y 2014 Isotropic magnetization response of electrodeposited nanocrystalline Ni–W alloy nanowire arrays *J. Appl. Electrochem.* **44** 301–7
- [39] Reddy S M, Park J J, Na S M, Maqableh M M, Flatau A B and Stadler B J H 2011 Electrochemical synthesis of magnetostrictive Fe–Ga/Cu multilayered nanowire arrays with tailored magnetic response *Adv. Funct. Mater.* **21** 4677–83
- [40] Elhoussine F, Vila L, Piroux L and Faini G 2005 Multiprobe perpendicular giant magnetoresistance measurements on isolated multilayered nanowires *J. Magn. Magn. Mater.* **290–291** 116–9
- [41] Takahashi M, Wakiyama T, Anayama T, Takahashi M and Suzuki T 1975 Magnetic anisotropy in Co and Co–Ni single crystals deformed by cold rolling *J. Phys. Soc. Jpn.* **38** 391–9
- [42] Kronmüller H 1985 The nucleation fields of uniaxial ferromagnetic crystals *Phys. Status Solidi b* **130** 197–203
- [43] Shakya P, Cox B and Davis D 2012 Giant magnetoresistance and coercivity of electrodeposited multilayered FeCoNi/Cu and CrFeCoNi/Cu *J. Magn. Magn. Mater.* **324** 453–9
- [44] Cox B, Davis D and Crews N 2013 Creating magnetic field sensors from GMR nanowire networks *Sensor. Actuator. A Phys.* **203** 335–40
- [45] Han J, Qin X, Quan Z, Wang L and Xu X 2016 Perpendicular giant magnetoresistance and magnetic properties of Co/Cu nanowire arrays affected by period number and copper layer thickness *Adv. Condens. Matter Phys.* **2016** 1–9
- [46] Mizoguchi S, Hayashida M and Ohgai T 2021 Determination of cobalt spin-diffusion length in Co/Cu multilayered heterojunction nanocylinders based on valet–fert model *Nanomaterials* **11** 218
- [47] Ide T, Hayashida M and Ohgai T 2021 Current-perpendicular-to-plane giant magnetoresistance in Co/Cu multilayered nanocylinders electrodeposited into anodized aluminum oxide nanochannels with ultra-large aspect ratio *J. Mater. Sci., Mater. Electron.* **32** 10089–100
- [48] Fan S, Zhou C, Xu H, Xu J, Wen H M, Xiao J Q and Hu J 2022 A novel strategy to improve giant magnetoresistance effect of Co/Cu multilayered nanowires arrays *J. Alloy. Compd.* **910** 164729